Current Optics and Photonics
Vol. 1, No. 3, June 2017, pp. 186-195

ISSN: 2508-7266(Print) / ISSN: 2508-7274(Online)
DOI: https://doi.org/10.3807/COPP.2017.1.3.186

Visibility Measurement in an Atmospheric Environment Simulation Chamber

Hongda Tai[1,2], Zibo Zhuang[1], Lihui Jiang[1], and Dongsong Sun[2]*

[1]*College of Air Traffic Mangement, Civil Aviation University of China, Tianjin 300300, China*
[2]*School of Earth and Space Sciences, University of Science and Technology of China, Hefei 230026, China*

(Received November 14, 2016 : revised March 9, 2017 : accepted March 24, 2017)

Obtaining accurate visibility measurements is a common atmospheric optical problem, and of vital significance to civil aviation. To effectively evaluate and improve the accuracy of visibility measurements, an outdoor atmospheric simulation chamber with dimensions of $1.8\times1.6\times55.7$ m^3 was constructed. The simulation chamber could provide a relatively homogeneous haze environment, in which the visibility varied from 10 km to 0.2 km over 5 hours. A baseline-changing visibility measurement system was constructed in the chamber. A mobile platform (receiver) was moved from 5 m to 45 m, stopping every 5 m, to measure and record the transmittance. The total least-squares method was used to fit the extinction coefficient. During the experiment conducted in the chamber, the unit weight variance was as low as 1.33×10^{-4} under high-visibility conditions, and the coefficient of determination (R^2) was as high as 0.99 under low-visibility conditions, indicating high stability and accuracy of the system used to measure the extinction coefficients and strong consistency between repeated measurements. A Grimm portable aerosol spectrometer (PAS) was used to record the aerosol distribution, and then Mie theory was used to calculate the extinction coefficients. The theoretical results were found to be consistent with the measurements and exhibited a positive correlation, although they were higher than the measured values.

Keywords : Aerosols, Atmospheric measurements, Laser measurement applications, Optical transmitters
OCIS codes : (010.1290) Atmospheric optics, (010.7295) Visibility and imaging, (290.2200) Extinction

I. INTRODUCTION

Visibility is a basic type of meteorological observation, and is the most important indicator for aviation in terms of aerodrome operating minima, flight-plan minima, and precision approach level.

Transmissometers and forward-scattering meters are the instruments recommended by ICAO to measure visibility [1, 2]. Transmissometers have been widely used as reference instruments in several published comparisons of visibility sensors [3-5], because of their direct measurement principle and relatively large sample volume. However, the accuracy of transmissometers is often too low to be desirable [5], and it is thus difficult to effectively evaluate their measurements.

Two main factors, the instrument itself and the atmospheric environment, affect the accuracy of visibility measurements:

1) The measurement error of a transmissometer can arise from incorrect alignment of transmitters and receivers, insufficient rigidity or stability of transmitter/receiver mountings, or fouling of the outer optical surface [6].
2) The variation and instability of real weather conditions can also contribute to visibility-measurement error. Because of the heterogeneous and turbulent nature of the atmosphere, the visibility of the environment is often nonuniform. Only if the atmosphere is homogeneous, and the extinction coefficient in the optical path of the instrument represents the actual extinction coefficient, can this error be reduced effectively.

Numerous publications have examined the correlation between visibility and various parameters, such as photo-source wavelength, liquid-water content (LWC), rain intensity, aerosol effective radius, and drop-size distribution (DSD)

*Corresponding author: sds@ustc.edu.cn
Color versions of one or more of the figures in this paper are available online.

[7-13]. All of these factors restrain each other, reducing the accuracy of visibility measurements.

Free-space laser communication (lasercom) is usually designed by estimating the atmospheric attenuation from visibility data in simulation chambers. Muhammad Ijaz et al. designed an indoor atmospheric laboratory chamber with dimensions of 550×30×30 cm^3 [13, 14]. Other large, outdoor atmospheric simulation chambers, such as AIDA [15], SAPHIR [16], EUPHORE [17] and UNC [18], have mainly been used to evaluate and study atmospheric chemical mechanisms. Furthermore, no large outdoor atmospheric simulation chamber has been specially designed to investigate the relationship between the atmospheric environment and visibility.

To improve the accuracy of visibility measurements and the assessment of measured results, baseline-changing measurements in a simulation chamber containing a homogeneous, stable atmosphere can be used. An outdoor atmosphere simulation chamber was constructed at Tianjin, China. A mobile platform was arranged in the chamber to measure the transmittance. Some characterization experiments have already been conducted to determine the extinction coefficient and visibility under various simulated atmospheric conditions.

II. EXPERIMENTAL SETUP

The experimental system was composed of an atmospheric environment simulation chamber, an observation and control room, an aerosol generator room, and an axial-flow fan room. Toughened glass was used to build the atmospheric environment simulation chamber. The schematic diagram of the haze simulation chamber is shown in Fig. 1(a). The simulation chamber has dimensions of 1.8×1.6×55.7 m^3, as depicted in Fig. 1(c), being as long as the a typical transmissometer with a baseline of 50 m. The subsystems for gas supply and circulation, mobile transmittance measurement, communication, monitoring, power supply, water supply, and drainage are the critical subsystems by which the experimental system normally runs.

The gas supply and circulation subsystem consists of one large axial-flow fan plus ten pairs of horizontal fans and ventilation ducts. The large axial-flow fan was installed in the axial-flow fan room to produce 0-5 m/s of adjustable axial wind, which can rapidly clear the chamber at the beginning and end of an experiment. The horizontal fans and ventilation ducts are located on one side of the chamber, as depicted in Fig. 1(b), to create local vortices. The horizontal fans and ventilation ducts run constantly during experiments, to ensure that the aerosols are homogeneously mixed.

The haze particles were produced by TOPAS ATM241, which generates polydisperse particles that are primarily smaller than 1 μm. The median value of the particle size generated by ATM241 was 0.5-1 μm. NaCl in deionized water was used as the aerosol liquid. The ATM241 and air compressor were placed in the aerosol generator room, and the particles were transmitted into the simulation chamber by the aerosol inlets, which were arranged every 5 m on one side of the chamber, as depicted in Fig. 1(d). The aerosol particles were suspended and then spread slowly

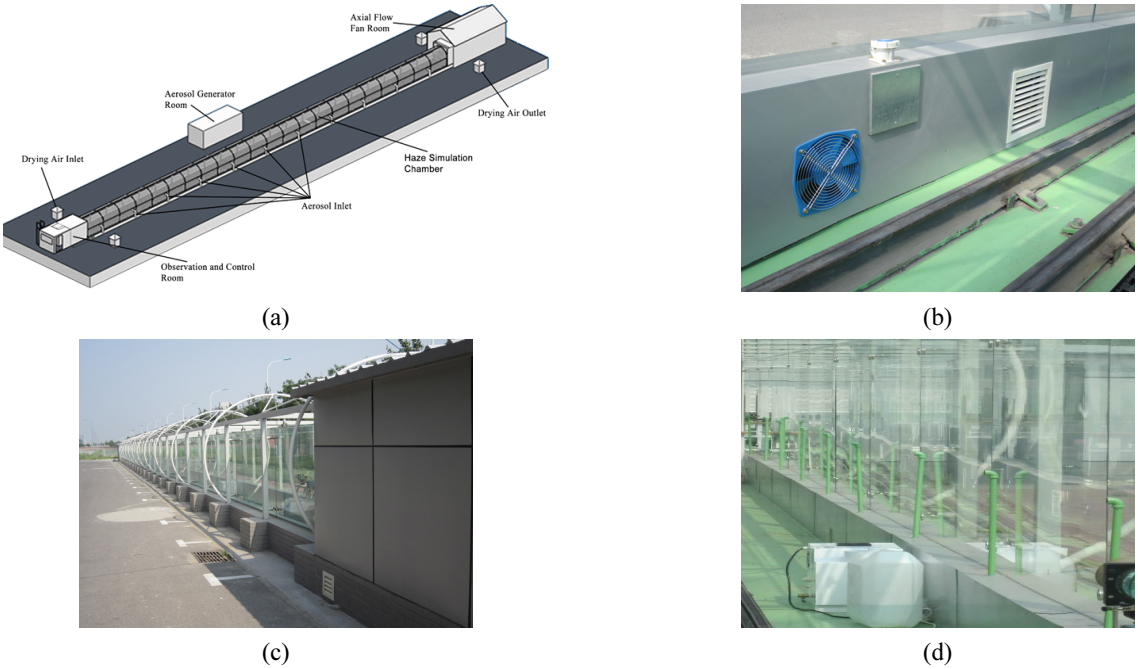

FIG. 1. (a) Schematic diagram of the atmospheric environment simulation chamber; (b) A horizontal fan and ventilation duct pair; (c) Photo of atmospheric environment simulation chamber; (d) The aerosol inlet inside the chamber.

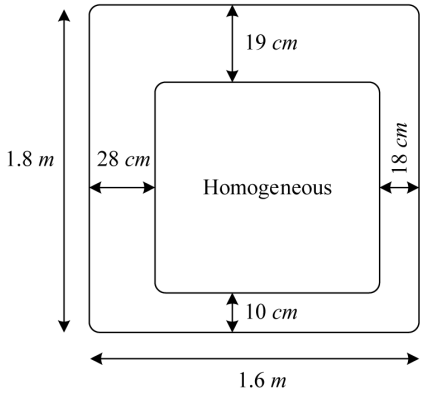

FIG. 2. Homogeneity within the chamber.

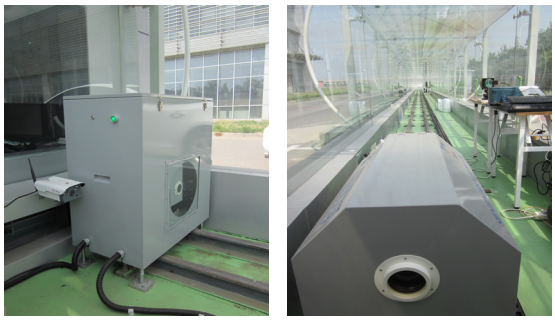

FIG. 3. The laser source and mobile platform.

within the chamber by the horizontal fans and ventilation ducts. The CFX simulation indicated that a relatively homogeneous atmospheric environment was finally formed in the center of the cross section, as depicted in Fig. 2.

A Grimm portable aerosol spectrometer PAS1.109 (0.25-32 μm in 31 size channels) was used to determine the particle concentration by size. The instrument was placed in the center of the chamber. The sampling time of the PAS1.109 can be set from 6 s to 60 min. The PAS sampled and recorded data throughout the experiment.

Figure 3 shows the mobile transmittance measurement subsystem. This subsystem consisted of a laser transmitter and receiver. A MSL-FN-532 with a wavelength of 532 nm was used as the laser source, and was fixed inside the transmitter next to the observation and control room. The photoelectric detector (THORLABS DET100A) and an industrial control computer were included on the mobile platform, to measure the extinction coefficient. The wavelength range of the photoelectric detector was 400-1100 nm. The receiver moved from 0 to 55 m at an adjustable speed (*e.g.* 0.4 m/s), stopping every 5 m and remaining motionless for 3 seconds to measure and record the data. Each round trip required a minimum of 2 minutes. The laser source wavelength was 532 ± 1 nm, and the power instability was less than 1% over 4 hours.

All control commands were sent by the server in the observation and control room. The measurement data of the receiver was transmitted to the server by a WLAN.

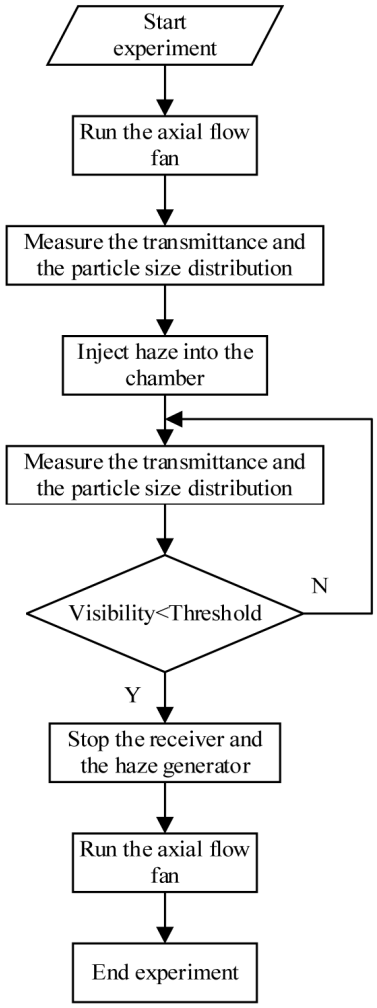

FIG. 4. Flow chart for the experiment.

Two network cameras were located at each end of the simulation chamber, to monitor the movement of the receiver and any changes in the simulation environment.

The flowchart for the experiment is given in Fig. 4. The visibility threshold in Fig. 4 is 200 m, considering all types of air-traffic operating indicators.

III. THEORETICAL BACKGROUND

3.1. Scattering Theory and Calculation of the Extinction Coefficient

The total extinction coefficient is composed of absorption and scattering terms. Generally, it is the following sum:

$$\sigma_{ext} = \sigma_{scat} + \sigma_{abs} = \sigma_{sm} + \sigma_{sa} + \sigma_{am} + \sigma_{aa} \quad (1)$$

where σ_{sm} and σ_{sa} are the molecular and aerosol scattering coefficients, and σ_{am} and σ_{aa} are the molecular and aerosol absorption coefficients.

Here we discuss the various existing expressions used in

calculating a fog/haze attenuation coefficient. Because the visible-light wavelengths occur within atmospheric transmission windows in the atmospheric absorption spectra, the contributions of absorption to the total attenuation coefficient are very small. As the fog/haze particle size approaches the visible-light wavelength (532 nm), the imaginary part of the refractive index of these particles is very small in this region of the spectrum. Molecular (Rayleigh) scattering is negligible, and Mie scattering by the aerosol particles thus becomes relatively dominant [19].

The scattering efficiency Q is defined as the scattering cross section normalized to the particle cross-sectional area [20]:

$$Q = \frac{C}{\pi r^2} \tag{2}$$

where r is the radius of the particle. Values for the scattering efficiency can be calculated using MiePlot, which is available online (http://www.philiplaven.com/mieplot.htm). As the radius of the particles increases, the scattering efficiency approaches 2.

Assuming independent scatterers and provided that multiple scattering is negligible, the total extinction coefficient σ can be calculated by summing the contributions from each aerosol particle size, based on the full Mie theory [9]:

$$\sigma \approx \sigma_{sa} = \sum_i n_i Q_i \pi r_i^2 \tag{3}$$

where n_i is the distribution or concentration of the i^{th} particle, Q_i is the scattering efficiency of the i^{th} particle, and r_i is the radius of the i^{th} particle.

The conversion of instrumental readings to the meteorological optical range and runway visual range is mainly based on Koschmieder's Law. The visual range is evaluated at 0.55 μm in practice, where the sensitivity of the human eye is maximal [9]. The pilot contrast threshold ε taken into account in Koschmieder's Law is 0.05 [21], which indicates that the visibility can be expressed in terms of the following equation, where σ is the total extinction coefficient:

$$Visibility = \frac{-\ln \varepsilon}{\sigma_{550}} \approx \frac{3}{\sigma_{532}} \tag{4}$$

To perform the full Mie calculation using Eq. (3), the aerosol particle size distribution must be known. In fact, it is the most important characteristic in determining the physical and optical properties of the atmosphere. A commonly used analytical size distribution model for aerosol particles is the Deirmendjian modified gamma distribution [22]:

$$n(r) = ar^{\alpha} \exp(-br^{\gamma}) \tag{5}$$

TABLE 1. Parameters of typical haze distributions

Distribution type	a	α	b	γ
Haze M	$5.333 \cdot 10^4$	1	8.9443	0.5
Haze L	$4.9757 \cdot 10^6$	2	15.1186	0.5
Haze H	$4.0 \cdot 10^4$	2	20	1

The differences in a, α, b and γ represent different particle size distributions, as is shown in Table 1. Haze M was first introduced to represent marine- or coastal-type distributions. Haze L has been adopted to represent continental-type aerosol distributions. Haze H can be used to represent high-level or stratospheric aerosols.

3.2. Baseline-changing Measurement and Total Least-squares Fitting

3.2.1. Baseline-changing Method

The attenuation of laser power through the atmosphere is described by the exponential Beer-Lambert law:

$$\tau(R) = \frac{P(R)}{P(0)} = e^{-\sigma \cdot R} \tag{6}$$

where $\tau(R)$ is the transmittance at range R, $P(R)$ is the laser power at R, $P(0)$ is the laser power at the light source, and σ is the total extinction coefficient.

To obtain the precise extinction coefficient, the mobile platform is used in the atmospheric simulation chamber according to the variable baseline method, as depicted in Fig. 5.

According to the Beer-Lambert law, the transmittance can be calculated as follows:

$$\begin{cases} \tau(R_1) = \dfrac{P(R_1)}{P(R_0)} = e^{-\sigma \cdot R_1} \\ \tau(R_2) = \dfrac{P(R_2)}{P(R_0)} = e^{-\sigma \cdot R_2} \\ \quad \vdots \quad \vdots \quad \vdots \\ \tau(R_n) = \dfrac{P(R_n)}{P(R_0)} = e^{-\sigma \cdot R_n} \end{cases} \tag{7}$$

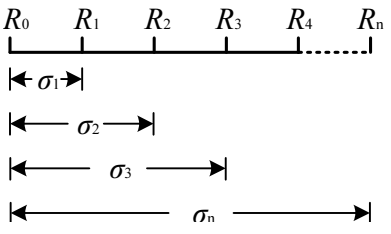

FIG. 5. Variable baseline model.

The logarithmic form of Eq. (7) is:

$$\ln \tau(R_i) = -\sigma \cdot R_i \quad (\mathrm{i} = 1,2,3,\cdots n) \tag{8}$$

The data array of R and ln τ can be obtained using the variable baseline method with the mobile platform, and then the extinction coefficients can be retrieved.

$$\begin{aligned} &\left[(R_1, \ln \tau_1),(R_2, \ln \tau_2),(R_3, \ln \tau_3),\cdots(R_n, \ln \tau_n)\right] \\ &\Rightarrow \left[\sigma_1, \sigma_2, \cdots \sigma_n\right] \end{aligned} \tag{9}$$

In the measurement, both $\ln \tau_n$ and R_n have errors, and as a result σ_n also has errors, according to Eq. (8). Fitting the extinction-coefficient array can return the precise extinction coefficient. In this paper, the total least-squares (TLS) method is used to fit the extinction-coefficient array.

3.2.2. TLS Method

The TLS method is suitable for regression equations in which the errors of the dependent and independent variables must be considered. In actual measurements, both the independent variable R_n and the dependent variable $\ln \tau_n$ inevitably contain errors. Therefore, the TLS method can be used when measuring the extinction coefficient σ.

A linear equation can be expressed as follows:

$$y_i = a x_i + b \quad (\mathrm{i} = 1,2,\cdots \mathrm{m}) \tag{10}$$

where a is the slope of the line, which corresponds to σ in this paper, and b is the intercept of the linear equation. a and b are the parameters to be estimated, and (x_i, y_i) are the surveying point's coordinates, corresponding to (Rn, ln τn). If a_0 and b_0 are the approximate values, then:

$$\begin{cases} a = a_0 + \delta a \\ b = b_0 + \delta b \end{cases} \tag{11}$$

The error equation can be expressed as follows:

$$v_{yi} = \begin{bmatrix} x_i & 1 \end{bmatrix} \begin{bmatrix} \delta a \\ \delta b \end{bmatrix} + (a_0 x_i + b_0 - y_i) \tag{12}$$

Eq. (13) is the error equation matrix expression:

$$A \delta X = l + V \tag{13}$$

where

$$A = \begin{bmatrix} x_1 & 1 \\ x_2 & 1 \\ \vdots & \vdots \\ x_m & 1 \end{bmatrix}, \quad l = \begin{bmatrix} a_0 x_1 + b_0 - y_1 \\ a_0 x_2 + b_0 - y_2 \\ \vdots \\ a_0 x_m + b_0 - y_m \end{bmatrix}, \quad V = \begin{bmatrix} v_{y1} \\ v_{y2} \\ \vdots \\ v_{ym} \end{bmatrix}, \quad \delta X = \begin{bmatrix} \delta a \\ \delta b \end{bmatrix}.$$

If we consider the error of the independent variable x in Eq. (10), the linear equation can be expressed as follows:

$$y_i + y_{yi} = \hat{a}(x_i + v_{xi}) + \hat{b} \quad (\mathrm{i} = 1,2,\cdots \mathrm{m}) \tag{14}$$

The error equation can be described in terms of the following formula by the EIV model [23]:

$$(A + E_A)\delta X = l + E_l \tag{15}$$

where EA is the error of the matrix and El is the error of the observation vector.

In matrix A, a column of the matrix element has a value of 1. Thus, matrix A can be expressed as

$$A = \begin{bmatrix} A_1 & A_2 \end{bmatrix} \tag{16}$$

where $A_1 = \begin{bmatrix} 1 & 1 & \cdots 1 \end{bmatrix}^{\mathrm{T}}$, $A_2 = \begin{bmatrix} x_1 & x_2 & \cdots x_m \end{bmatrix}^{\mathrm{T}}$.

If the augmented matrix $C = \begin{bmatrix} A & l \end{bmatrix}$, then the QR decomposition of the augmented matrix C can be written as

$$C = QR \tag{17}$$

where Q is an orthogonal matrix and R is a triangular matrix:

$$R = Q^{\mathrm{T}} C = Q^{\mathrm{T}} \begin{bmatrix} A_1 & A_2 & l \end{bmatrix} = \begin{bmatrix} R_{11} & R_{12} & R_{1l} \\ 0 & R_{22} & R_{2l} \end{bmatrix}^{1}_{2} \tag{18}$$

If the augmented matrix $C_R = \begin{bmatrix} R_{22} & R_{2l} \end{bmatrix}$, singular-value decomposition (SVD) of CR can be written as

$$C_R = U \sum N^{\mathrm{T}} \tag{19}$$

where $U = \begin{bmatrix} \underbrace{U_1}_{2\times1} & \underbrace{U_2}_{2\times1} \end{bmatrix}$, $N = \begin{bmatrix} \underbrace{N_1}_{2\times1} & \underbrace{N_2}_{2\times1} \end{bmatrix}$, $\sum = diag(\sigma_1, \sigma_2)$.

Then,

$$\begin{bmatrix} \delta \hat{a} \\ \delta \hat{b} \end{bmatrix} = \left(A^{\mathrm{T}} A - \sigma_2^2 \begin{bmatrix} 0 & 0 \\ 0 & 1 \end{bmatrix} \right)^{-1} A^{\mathrm{T}} l \tag{20}$$

The range correction of the augmented matrix CR can be written as

$$E_{C_R} = \sigma_2 U_2 N_2^{\mathrm{T}} \tag{21}$$

The range correction of matrix R can be written as

$$E_R = \begin{bmatrix} 0 & 0 \\ 0 & E_{C_R} \end{bmatrix} \tag{22}$$

The range correction of matrix A and observation vector l can be written as

$$\begin{bmatrix} E_A & E_l \end{bmatrix} = \begin{bmatrix} E_{A_1} & E_{A_2} & E_l \end{bmatrix} = Q^{\mathrm{T}} E_R \tag{23}$$

Then, the residual errors in the x- and y-axes can be written as

$$\begin{cases} v_x = E_{A_2} \\ v_y = E_l \end{cases} \tag{24}$$

The orthogonal distance residuals of $v_{si} = \sqrt{v_{xi}^2 + v_{yi}^2}$ are depicted in Fig. 6.

To minimize the sum of the residual of squares, TLS uses the orthogonal distance criterion:

$$F_{TLS} = v_s^{\mathrm{T}} v_s = v_x^{\mathrm{T}} v_x + v_y^{\mathrm{T}} v_y \tag{25}$$

The accuracy of the data fitting should be in accordance with the residual orthogonal distance. The unit weight variance can be expressed as follows:

$$\sigma_{TLS} = \sqrt{\frac{F_{TLS}}{m-2}} \tag{26}$$

TLS can reduce the measurement error due to the device, and other nonlinear factors introduced by the design principles. This method can improve the measurement accuracy of the extinction coefficient.

The coefficient of determination R^2, which is also called the multiple correlation coefficient, can be used to evaluate the effect of the fitting [24]. Its definition as the proportion of variance explained by the regression model makes it useful as a measure of the success of predicting the dependent variable from the independent variables. The following definition was used for R^2:

$$R^2 = \frac{\sum_{i=1}^{n} w_i (\hat{y}_i - \overline{y}_i)^2}{\sum_{i=1}^{n} w_i (y_i - \overline{y}_i)^2} \tag{27}$$

A good fit is indicated by an R^2 value close to 1.

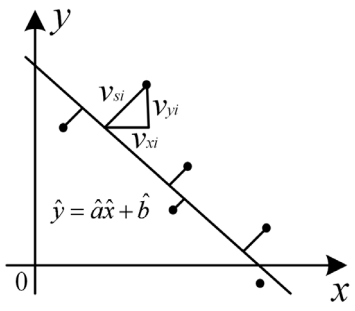

FIG. 6. Geometrical distance of TLS.

IV. EXPERIMENTAL RESULTS AND DATA ANALYSES

4.1. Experimental Setting

Our experiment was conducted on 4/23/2015 from 21: 13:00 GMT+8 to 01:31:00 GMT+8. The aerosol generator ATM241 continuously sprayed small droplets into the simulation chamber. The visibility decreased from approximately 6200 m to 190 m. The PAS sampling time was set to 5 minutes to record the aerosol distribution. The mobile platform moved back and forth during the whole experiment. The speed of the receiver was set to 0.4 m/s. Thus the mobile platform required 10 minutes to run two rounds, during which the aerosol concentration and distribution were considered to be the same. As a result, the transmittance was measured 4 times every 5 m. During the experiment, the temperature and pressure were maintained at relatively stable levels. The relative humidity increased because of the continuous aerosol spray into the simulation chamber. The temperature and relative humidity are plotted in Fig. 7.

4.2. Extinction-coefficient Data Fitting

As mentioned in section 4.1, the receiver measured and recorded the transmittance 4 times at every measurement point every 10 minutes. As an example, the transmittance recorded during the last 10 minutes of the experiment is shown in Table 2.

All of the transmittance data measured during the experiment were recorded as the visibility declined. Figure 10 depicts the relationship between the logarithm of the transmittance and the baseline measurements. The extinction coefficient and the corresponding visibility were calculated

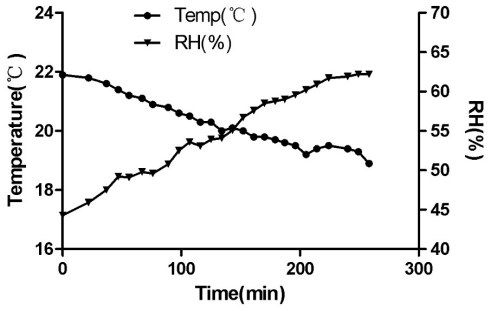

FIG. 7. Temperature and relative humidity evolution in the chamber.

TABLE 2. Transmittance measured at a visibility of 194.4 m.

Baseline (m)	5	10	15	20	25
Round 1 forth	0.953188	0.909844	0.852437	0.79214	0.726257
Round 1 back	0.95307	0.91396	0.862336	0.802784	0.731245
Round 2 forth	0.957578	0.919013	0.854994	0.797339	0.723679
Round 2 back	0.959144	0.907882	0.860667	0.797649	0.72673
Baseline (m)	30	35	40	45	
Round 1 forth	0.657677	0.59449	0.533423	0.485263	
Round 1 back	0.670147	0.598608	0.551431	0.499807	
Round 2 forth	0.659275	0.595256	0.538373	0.483031	
Round 2 back	0.665446	0.598381	0.534978	0.496242	

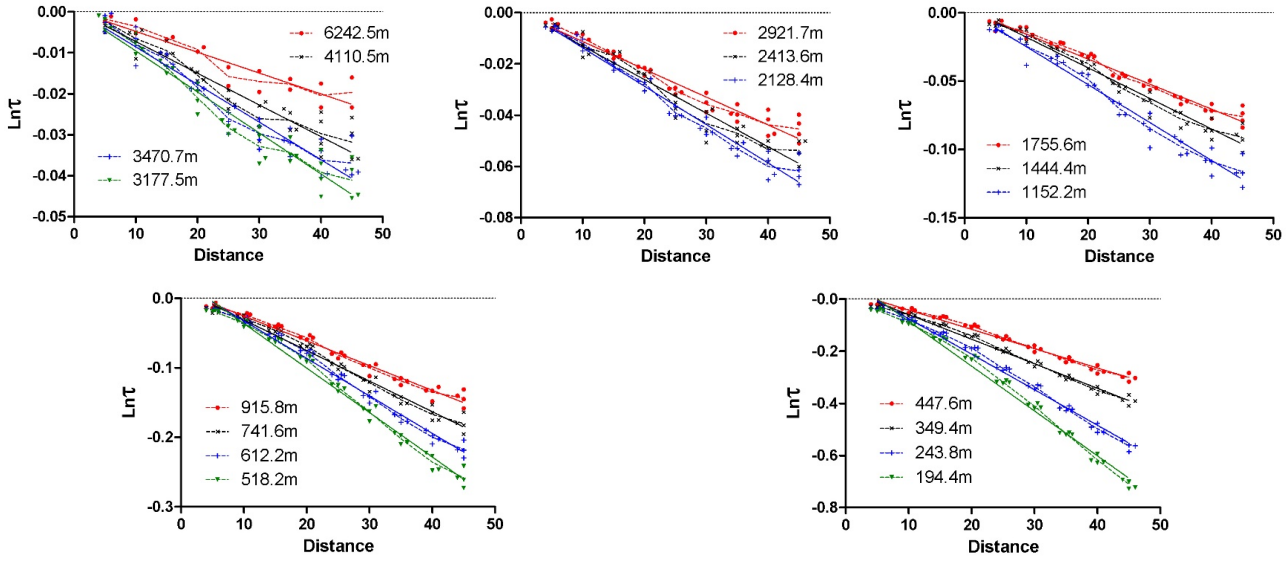

FIG. 8. Transmittance measurement results under different visibility conditions: (a) Visibility exceeding 3000 m. (b) Visibility between 2000 m and 3000 m. (c) Visibility between 1000 m and 2000 m. (d) Visibility between 500 m and 1000 m. (e) Visibility between 150 m and 500 m.

using Eq. (8) and the TLS method. The dashed lines in Fig. 8 show the mean values of the logarithm of the transmittance when the receiver was at different distances from the transmitter. The slopes of the solid lines, which were obtained by the TLS method, indicate the extinction coefficients. The corresponding visibility can be calculated using Koschmieder's Law. Four different cases of visibility exceeding 3000 m are depicted in Fig. 8(a), and three different cases of visibility between 2000 m and 3000 m are shown in Fig. 8(b). Fig. 8(c) shows three different cases of visibility between 1000 m and 2000 m. Figure 8(d) shows four different cases of visibility between 500 m and 1000 m, and Fig. 8(e) shows four different cases of visibility between 190 m and 500 m.

4.3. System Performance Analysis

The unit-weight variance and coefficient of determination under different visibilities could be calculated using Eqs. (26) and (27), as depicted in Table 3. As the aerosol concentration increases, the extinction coefficients also increase, whereas the visibility decreases. Because the true value of the visibility is impossible to obtain, the unit-weight variance of the extinction can be used to indicate the deviation between the measured value and the true value. The coefficients of determination are mostly greater than 0.9, especially when the visibility is less than 5000 m. When the visibility is less than 1000 m, the coefficients of determination are all above 0.98. The larger coefficients of determination indicate the high stability of this system in measuring extinction coefficients, and the high consistency of repeated experiments.

The extinction coefficient increases and the visibility decreases as the aerosol concentration increases. When the visibility exceeds 3000 m, the extinction coefficients are relatively small. As a result, the unit-weight variances of the extinction coefficient are mainly less than 5×10^{-4},

TABLE 3. Unit-weight variance and coefficient of determination under different visibilities.

Visibility (m)	Above 3000 m				2000-3000 m			1000-2000 m	
	6242.5	4110.5	3470.7	3177.5	2921.7	2413.6	2128.4	1755.6	1444.4
Unit weight variance (10^{-4})	1.33	4.34	4.43	4.64	3.87	3.87	4.21	5.45	11.1
Coefficient of determination	0.854	0.8923	0.9193	0.9283	0.9481	0.939	0.9697	0.9736	0.9644
Visibility (m)		500-1000 m				150-500 m			
	1152.2	915.8	741.6	612.2	518.2	447.6	349.4	243.8	194.4
Unit weight variance (10^{-4})	18.81	15.36	22.99	21.51	37.27	46.69	48.94	114.4	219.7
Coefficient of determination	0.9609	0.9802	0.9806	0.9878	0.9851	0.986	0.9909	0.9898	0.9878

which are much smaller than those at low visibility, *e.g.* 1444.4 m in Table 3. However, the background light and other factors greatly affect transmittance measurements. The coefficient of determination is also lower than those at low visibility, mostly below 0.93. As the visibility decreases, the extinction coefficients and corresponding unit-weight variances increase. Because there is less influence from outside factors, the coefficient of determination gradually increases. When the visibility is less than 1000 m, coefficients of determination higher than 0.98 clearly indicate the very good performance of this system.

4.4. Aerosol particle size distribution

In the experiment, the particle size distribution was measured as the sum of the particle number concentration observed in all channels, in terms of sphere counts. The particle number variations at sizes of 0.5 μm, 1 μm, 2 μm and 2.5 μm recorded by PAS during the experiment are plotted in Fig. 9. Because the particles produced by TOPAS ATM241 are mainly smaller than 1 μm, the number of 0.5-μm aerosols increases consistently. The number of 1-μm aerosols remains unchanged during the initial period, and then grows rapidly during the experiment. This may be due to the collisions of small particles, resulting in coalescence and growth to 1 μm. The number of larger particles (2 μm and 2.5 μm) grows much more slowly than that of smaller particles, as depicted in Fig. 9. The number of larger particles shows little change during the whole experiment.

Fig. 10 depicts the evolution of the haze particle number

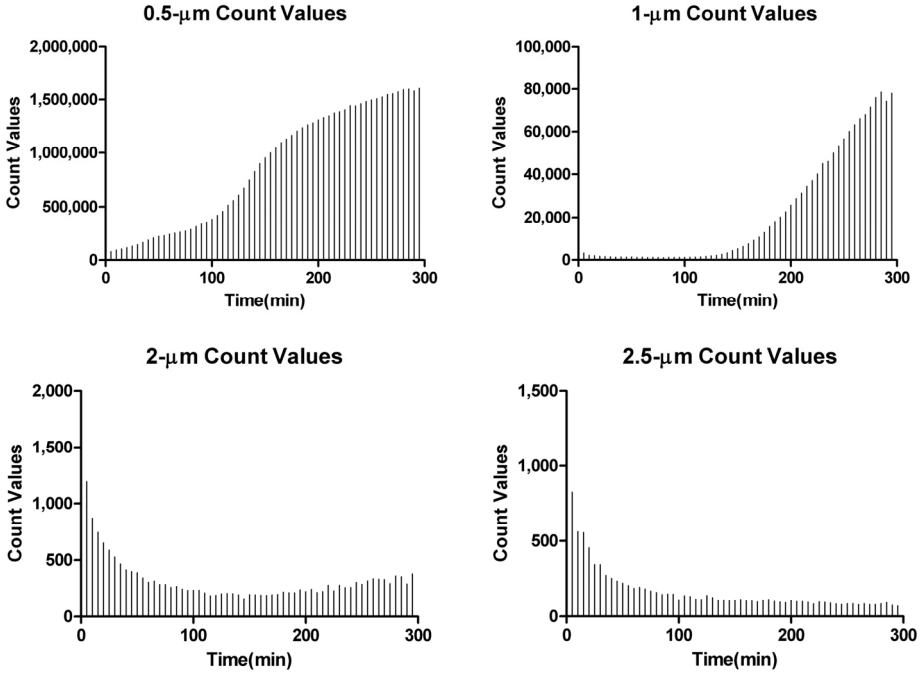

FIG. 9. Particle number variation versus time.

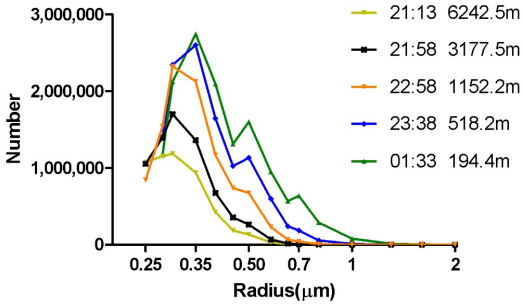

FIG. 10. Particle size distribution.

distribution during the whole experiment, using logarithmic coordinates. As small particles are sprayed into the chamber, the total number of aerosol particles increases, but the numbers of different-sized aerosol particles do not show linear increases. As the aerosol concentration increases, the maximum abscissa of the curve, which is also called the model radius, increases. The peak aerosol number concentrations gradually narrow to 0.35 μm, 0.5 μm, and 0.7 μm.

V. FULL MIE CALCULATION

The aerosol spectrometer PAS1.109 was used to measure the aerosol particle size distributions. The particle size distributions in the haze chamber were essentially consistent with the Deirmendjian modified gamma distributions. We assume that the scattering particle size distribution in the atmospheric simulation chamber corresponded exactly to the Deirmendjian modified gamma distribution. The particle size distribution in the chamber can be obtained according to the analyzed positive and real constants a, b, and γ, and the integer α. MiePlot was used to calculate the scattering efficiencies as a function of particle diameter, for particles made of water (refractive index 1.33) scattering 532-nm light. The total scattering σ can then be calculated by summing the contributions from each particle size, using Eq. (3).

The aerosol-derived visibilities are too high relative to the directly measured ones. This conclusion is consistent with that of D. Baumer *et al.* [25], but the possible explanations are different. Because all of the experimental data were obtained from the atmospheric simulation chamber, their representative nature is not the critical issue. One possible explanation is that the absorption of aerosols was underestimated. Additionally, the Deirmendjian modified gamma distribution could not be validated using the experimental data.

VI. CONCLUSION

Visibility is a crucial meteorological parameter in many fields, and it is very important to accurately measure visibility, especially in aerodromes.

A large atmospheric simulation chamber was constructed by the Civil Aviation University of China in Tianjin. Controllable simulated haze with visibility as low as 200 m can be achieved within 5 hours. A mobile platform was included in the chamber to measure the atmospheric transmittance. The extinction coefficient and corresponding visibility were obtained using this system. Repeated experiments demonstrated the system's high stability, accuracy, and consistency. The analysis of the particle size distribution and the full Mie calculation contribute to determining the relationship between visibility and aerosol particle size distribution, to some degree.

Future research will address the relationships between the laser wavelength, relative humidity, liquid water content, the modal radius of aerosols, and visibility under environmental conditions with different chemical constituents in the atmospheric environment simulation chamber.

ACKNOWLEDGMENT

This work was supported by the National Science Foundation of China (No. U1533113, U1433202, 41227804 and 41174130).

REFERENCES

1. I. C. A. Organization, *Manual on Automatic Meteorological Observing Systems at Aerodromes*, (International Civil Aviation Organization, Montreal, CA, 2013).
2. I. C. A. Organization, *Manual of Runway Visual Range Observing and Reporting Practices*, (International Civil Aviation Organization, Montreal, CA, 2005).
3. D. J. Griggs, D. W. Jones, M. Ouldridge, and W. R. Sparks, *The first WMO intercomparison of visibility measurements*, (World Meteorological Organization, Geneva, Switzerland, 1990).
4. H. I. Bloemink, "KNMI visibility standard for calibration of scatterometers," in *WMO Technical Conference on Instruments and Methods of Observation* (Geneva, Switzerland, 2006), pp.4-6.
5. J. D. Crosby, "Visibility sensor accuracy: what's realistic," in *12th Sympsium on Meterological Observations and Instrumentation* (Long Beach, CA, Feb.2003), pp.9-13.
6. W. M. Organization, *Guide to Meterological Instruments and Methods of Observation* (Secretariat of the World Meteorological Organization, Geneva, Switzerland, 2008).
7. I. I. Kim, B. McArthur, and E. J. Korevaar, "Comparison of laser beam propagation at 785 nm and 1550 nm in fog and haze for optical wireless communications," Proc. SPIE **4214**, 26-37 (2001).
8. M. Al Naboulsi, "Fog attenuation prediction for optical and infrared waves," Optical Engineering **43**, 319-329 (2004).
9. R. Nebuloni, "Empirical relationships between extinction coefficient and visibility in fog," Applied Optics **44**, 3795-3804 (2005).

10. K. W. Fischer, M. R. Witiw, and E. Eisenberg, "Optical attenuation in fog at a wavelength of 1.55 micrometers," Atmospheric Research **87**, 252-258 (2008).
11. E. Ferdinandov, K. Dimitrov, A. Dandarov, and I. Bakalski, "A general model of the atmospheric scattering in the wavelength interval 300-1100 nm," Radioengineering **18**, 517-521 (2009).
12. M. Grabner and V. Kvicera, "The wavelength dependent model of extinction in fog and haze for free space optical communication," Optics Express **19**, 3379-3386 (2011).
13. M. Ijaz, Z. Ghassemlooy, J. Pesek, O. Fiser, H. Le Minh, and E. Bentley, "Modeling of fog and smoke attenuation in free space optical communications link under controlled laboratory conditions," Journal of Lightwave Technology **31**, 1720-1726 (2013).
14. Z. Ghassemlooy, H. Le Minh, S. Rajbhandari, J. Perez, and M. Ijaz, "Performance analysis of Ethernet/fast-Ethernet free space optical communications in a controlled weak turbulence condition," Journal of Lightwave Technology **30**, 2188-2194 (2012).
15. O. Möhler, S. Büttner, C. Linke,M. Schnaiter, H. Saathoff, O. Stetzer,R. Wagner, M. Krämer, A. Mangold, V. Ebert, and U. Schurath, "Effect of sulfuric acid coating on heterogeneous ice nucleation by soot aerosol particles," Journal of Geophysical Research Atmospheres **110**, 1423-1436 (2005).
16. T. Brauers, B. Bohn, F. J. Johnen, R. Rohrer, S. Rodriguez Bares, R. Tillmann, and A. Wahner, "The atmosphere simulation chamber saphir: a tool for the investigation of photochemistry," EGS-AGU-EUG Joint Assembly **1**, 4449 (2003).
17. K. H. Becker, "The European Photoreactor EUPHORE, final report of the EC-Project," Contract EV5V-CT92, **59** (1996).
18. H. Jeffries, D. Fox, and R. Kamens, "Outdoor smog chamber studies: light effects relative to indoor chambers," Environmental Science & Technology **10**, 1006-1011 (1976).
19. E. J. McCartney, and F. F. Hall, *Optics of the Atmosphere: Scattering by Molecules and Particles* (John Wiley and Sons, New York, USA, 1977).
20. P. W. Kruse, L. D. McGlauchlin, and R. B. McQuistan, *Elements of Infrared Technology: Generation, Transmission, and Detection* (Wiley, New York, USA, 1962).
21. I. C. A. Organization, *Annex 3 to the Convention on International Civil Aviation. Meteorological Service for International Air Navigation* (International Civil Aviation Organization, Montreal, CA, 2013).
22. D. Deirmendjian, *Electromagnetic scattering on spherical polydispersions* (American Elsevier Publishing Company Inc., New York, USA, 1969).
23. S. V. Huffel and J. Vandewalle, "The Total Least Squares Problem: Computational Aspects and Analysis," Mathematics of Computation **59**, 200 (1991).
24. B. R. Rao, S. Mazumdar, J. H. Waller, and C. C. Li, "Correlation between the numbers of two types of children in a family," Biometrics **29**, 271-279 (1973).
25. D. Bäumer, B. Vogel, S. Versick, R. Rinke, O. Möhler, and M. Schnaiter, "Relationship of visibility, aerosol optical thickness and aerosol size distribution in an ageing air mass over South-West Germany," Atmospheric Environment **42**, 989-998 (2008).